Mon. Not. R. Astron. Soc. **000**, 1–?? (2011) Printed 7 May 2012 (MN LaTeX style file v2.2)

arXiv:1112.0330v2 [astro-ph.CO] 4 May 2012

Nonlinear evolution of cosmological structures in Warm Dark Matter models

Aurel Schneider[1]⋆, Robert E. Smith[1,2], Andrea V. Macciò[3], and Ben Moore[1]

[1] *Institute for Theoretical Physics, University of Zurich, Zurich CH 8057*
[2] *Argelander-Institute for Astronomy, Auf dem Hügel 71, D-53121 Bonn, Germany*
[3] *Max Planck Institut für Astronomie, Königsstuhl 17, D-69117 Heidelberg, Germany*

7 May 2012

ABSTRACT

The dark energy dominated warm dark matter (WDM) model is a promising alternative cosmological scenario. We explore large-scale structure formation in this paradigm. We do this in two different ways: with the halo model approach and with the help of an ensemble of high resolution N-body simulations. Combining these quasi-independent approaches, leads to a physical understanding of the important processes which shape the formation of structures. We take a detailed look at the halo mass function, the concentrations and the linear halo bias of WDM. In all cases we find interesting deviations with respect to CDM. In particular, the concentration-mass relation displays a turnover for group scale dark matter haloes, for the case of WDM particles with masses of the order $m_{\rm WDM} \sim 0.25$keV. This may be interpreted as a hint for top-down structure formation on small scales. We implement our results into the halo model and find much better agreement with simulations. On small scales the WDM halo model now performs as well as its CDM counterpart.

Key words: Cosmology: theory - large-scale structure of the Universe - dark matter

1 INTRODUCTION

Over the last decade the vacuum energy dominated cold dark matter (hereafter ΛCDM) scenario, has emerged as a standard model for cosmology. This owes largely to the combination of information from galaxy clustering surveys such as the 2dFGRS and SDSS with WMAP measurements of the temperature anisotropies in the microwave background (Cole et al. 2005; Tegmark et al. 2006; Komatsu et al. 2011). However, the nature of the two dark components in the ΛCDM model are still completely unknown and it is therefore important to keep exploring alternative models and test their compatibility with observations.

In the ΛCDM model the dark matter is assumed to be composed of heavy, cold thermal relic particles that decoupled from normal matter very early in the history of the Universe (Peebles 1982; Blumenthal et al. 1984; Kolb & Turner 1990; Jungman et al. 1996). Whilst there is a large body of indirect astrophysical evidence that strongly supports CDM, there are some hints that it has shortcomings. Firstly, CDM galaxy haloes contain a huge number of subhaloes (Moore et al. 1999; Diemand & Kuhlen 2008; Springel et al. 2008; Stadel et al. 2009), while observations indicate that only relatively few satellite galaxies exist around the Milky Way and M31 (Moore et al. 1999; Klypin et al. 1999). Secondly, the highest resolution halo simulations show that the slope of the inner density profile decreases linearly at smaller radii (Navarro et al. 1997; Moore et al. 1999; Diemand et al. 2004; Springel et al. 2008; Stadel et al. 2009), whereas the density profiles inferred from galaxy rotation curves are significantly shallower (Moore et al. 1999) (and for recent studies see Swaters et al. 2003; Salucci et al. 2007; de Blok et al. 2008; Gentile et al. 2009, and references there in). Thirdly, the observed number of dwarf galaxies in the voids appears to be far smaller than expected from CDM (Peebles 2001; Tikhonov et al. 2009; Peebles & Nusser 2010). Another example is the excess in the prediction of dwarf galaxy concentrations (Lovell et al. 2011). Whilst, it has become clear that some of these discrepancies might be resolved through an improved understanding of galaxy formation, they have led some to consider changes to the ΛCDM paradigm.

One possible solution might be warm dark matter (WDM) (Bond & Szalay 1983; Bardeen et al. 1986; Bode et al. 2001). In this scenario, the dark particle is considered to be lighter than its CDM counterpart, and so remains relativistic longer and also retains a thermal velocity. Since WDM particles are collisionless and decouple early, they may ‘free-stream’ or diffuse out of perturbations whose

---

⋆ Email: aurel@physik.uzh.ch

size is smaller than the Jeans' length[1] in the radiation dominated Universe (Kolb & Turner 1990). This free-streaming of the WDM particles acts to damp structure formation on small scales. Two potential candidates are the sterile neutrino (Dodelson & Widrow 1994; Shaposhnikov & Tkachev 2006), and the gravitino (Ellis et al. 1984; Moroi et al. 1993; Kawasaki et al. 1997; Gorbunov et al. 2008), both of which require extensions of the standard model of particle physics.

Recent observational constraints have suggested that sterile neutrinos can not be the dark matter: the Lyman alpha forest (Seljak et al. 2006; Boyarsky et al. 2009a) and QSO lensing (Miranda & Macciò 2007) bounds are $m_{\nu_s} > 8\text{keV}$, whilst those from the X-ray background are $m_{\nu_s} < 4\text{keV}$ (Boyarsky et al. 2008)[2]. However, a more recent assessment has suggested that a better motivated particle physics model based on resonant production of the sterile neutrino, may evade these constraints: the Lyman alpha forest bound is brought down to $m_{\nu_s} \gtrsim 2\text{keV}$ and the X-ray background is pushed to $m_{\nu_s} < 50\text{keV}$ (for very low mixing angles) (Boyarsky et al. 2009b). It therefore seems that additional, independent methods for constraining the ΛWDM scenario would be valuable.

In Markovic et al. (2010) and Smith & Markovic (2011), it was proposed that the ΛWDM scenario could be tested through weak lensing by large-scale structure. The advantage of such a probe is that it is only sensitive to the total mass distribution projected along the line of sight. However, to obtain constraints on the WDM particle mass, an accurate model for the nonlinear matter clustering is required. In these papers, an approach based on the halo model was developed. Accurate predictions from this model require: detailed knowledge of the abundance of dark matter haloes, their spatial large-scale bias, and their density profiles. In these studies, it was assumed that the semi-analytic methods, which were developed for CDM, would also apply to WDM.

In this paper we perform a series of very high resolution CDM and WDM N-body simulations with the specific aim of exploring the halo model ingredients in the ΛWDM scenario. Over the past decade, there have been a limited number of numerical simulation studies of nonlinear structure formation in the WDM model (Colombi et al. 1996; Moore et al. 1999; Colín et al. 2000; White & Croft 2000; Avila-Reese et al. 2001; Bode et al. 2001; Bullock et al. 2002; Zentner & Bullock 2003; Colín et al. 2008; Zavala et al. 2009; Macciò & Fontanot 2010; Lovell et al. 2011; Viel et al. 2011; Dunstan et al. 2011). In most of these previous studies, conclusions have been drawn from object-by-object comparison of a relatively small number of haloes simulated in boxes of typical size $L = 25\,h^{-1}\text{Mpc}$. In this work we are more interested in the overall impact that the WDM hypothesis has on the statistical properties of large-scale structures. We therefore simulate boxes that are 10 times larger than have been typically studied before, hence having roughly ~ 1000 times larger sampling volume. This means, that our conclusions will have greater statistical weight, than those from previous studies. Furthermore, our results should be less susceptible to finite volume effects, which can lead to underestimates of the nonlinear growth.

The paper is structured as follows: In §2 we provide a brief overview of the salient features of linear theory structure formation in the WDM model and we review the halo model approach. In §3 we describe the N-body simulations. In §4 we explore the main ingredients of the halo model: the halo mass function, bias and density profiles. In §5 we compare the halo model predictions for the matter power with our measurements from the simulations. Finally, in §6 we summarize our findings.

2 THEORETICAL BACKGROUND

In this section we summarize the linear theory for WDM and the nonlinear halo model in this framework.

2.1 Linear theory evolution of WDM

The physics of the free-streaming or diffusion of collisionless particles out of dark matter perturbations has been discussed in detail by Bond & Szalay (1983)[3]. An estimate for the free-streaming length can be obtained, by computing the comoving length scale that a particle may travel up until matter-radiation equality ($t_{\rm EQ}$). At this point, the Jeans' length drops dramatically and perturbations may collapse under gravity. A simple formula for this is given by Kolb & Turner (1990):

$$\lambda_{\rm fs} = \int_0^{t_{\rm EQ}} \frac{v(t)dt}{a(t)} \approx \int_0^{t_{\rm NR}} \frac{c dt}{a(t)} + \int_{t_{\rm NR}}^{t_{\rm EQ}} \frac{v(t)dt}{a(t)} \ , \tag{1}$$

where $t_{\rm NR}$ is the epoch when the WDM particles become non-relativistic, which occurs when $T_{\rm WDM} < m_{\rm WDM}c^2/3k_{\rm B}$, where $T_{\rm WDM}$ and $m_{\rm WDM}$ are the characteristic temperature and mass of the WDM particles. In the relativistic case, the mean peculiar velocity of the particle is simply $v(t) \sim c$. In the non-relativistic regime its momentum simply redshifts with the expansion: $v \propto a(t)^{-1}$. This leads to:

$$\lambda_{\rm fs} \approx r_{\rm H}(t_{\rm NR}) \left[1 + \frac{1}{2}\log\frac{t_{\rm EQ}}{t_{\rm NR}}\right] \ , \tag{2}$$

where $r_{\rm H}(t_{\rm NR})$ is the comoving size of the horizon at $t_{\rm NR}$. On inserting typical values for $t_{\rm NR}$ we find the scaling:

$$\lambda_{\rm fs} \quad \approx \quad 0.4 \left(\frac{m_{\rm WDM}}{\rm keV}\right)^{-4/3} \left(\frac{\Omega_{\rm WDM}h^2}{0.135}\right)^{1/3} \left[h^{-1}{\rm Mpc}\right] \tag{3}$$

However, the real situation is more complex than this, since fluctuations inside the horizon grow logarithmically during radiation domination via the Meszaros effect and free-streaming does not switch off immediately after $t_{\rm EQ}$. To understand the collisionless damping in more detail, one must numerically solve the coupled Einstein-Boltzmann system of equations for the various species of matter and radiation.

---

[1] Although originally defined in the context of gas dynamics, the Jeans length can be generalized to collisionless systems by replacing the sound speed with the velocity dispersion. The reason for this tight analogy lies in the linearized equation of perturbations, which has the same structure for gas and collisionless fluids (see Peebles 1982, for more details).

[2] Lower bounds on the mass of a fully thermalized WDM particle can be obtained using Eq. (6) (see Viel et al. 2005).

[3] For some recent theoretical treatments of WDM, also see Boyanovsky (2010) and de Vega & Sanchez (2010, 2011)

Several fitting formulae for the WDM density transfer function have been proposed (Bardeen et al. 1986; Bode et al. 2001) and here we adopt the formula in Viel et al. (2005):

$$T_{\rm WDM}(k) = \left[\frac{P_{\rm lin}^{\rm WDM}}{P_{\rm lin}^{\rm CDM}}\right]^{1/2} = \left[1+(\alpha k)^{2\mu}\right]^{-5/\mu} , \tag{4}$$

with $\mu = 1.12$ as well as

$$\alpha = 0.049 \left[\frac{m_{\rm WDM}}{\rm keV}\right]^{-1.11} \left[\frac{\Omega_{\rm WDM}}{0.25}\right]^{0.11} \left[\frac{h}{0.7}\right]^{1.22} {\rm Mpc/h}. \tag{5}$$

Note that in the above we are assuming that the WDM particle is fully thermalized. Following Viel et al. (2005), the masses of sterile neutrino WDM particles m_{ν_s} can be obtained from $m_{\rm WDM}$ through the formula:

$$m_{\nu_s} = 4.43{\rm keV} \left(\frac{m_{\rm WDM}}{1{\rm keV}}\right)^{4/3} \left(\frac{w_{\rm WDM}}{0.1225}\right)^{-1/3} . \tag{6}$$

The characteristic length-scale α is related to the free-streaming scale $\lambda_{\rm fs}$, and we shall therefore make the definition that $\alpha \equiv \lambda_{\rm fs}^{\rm eff}$ is an *effective* free-streaming length scale. The length-scale $\lambda_{\rm fs}^{\rm eff}$ can be used to introduce the 'free-streaming' mass scale:

$$M_{\rm fs} = \frac{4\pi}{3}\bar{\rho}\left(\frac{\lambda_{\rm fs}^{\rm eff}}{2}\right)^3 , \tag{7}$$

where $\bar{\rho}$ is the background density of the universe. This mass scale is important as it defines the scale below which initial density perturbations are completely erased.

We can define yet another length scale: the 'half-mode' length scale $\lambda_{\rm hm}$. This corresponds to the length scale at which the amplitude of the WDM transfer function is reduced to 1/2. From Eq. (4) we find:

$$\lambda_{\rm hm} = 2\pi\lambda_{\rm fs}^{\rm eff}\left(2^{\mu/5}-1\right)^{-1/2\mu} \approx 13.93\lambda_{\rm fs}^{\rm eff} . \tag{8}$$

This length scale leads us to introduce another mass scale, the half-mode mass scale:

$$M_{\rm hm} = \frac{4\pi}{3}\bar{\rho}\left(\frac{\lambda_{\rm hm}}{2}\right)^3 \approx 2.7\times 10^3 M_{\rm fs} . \tag{9}$$

This mass scale is where we expect the WDM to first affect the properties of dark matter haloes. In passing, this partly explains the claims made by Smith & Markovic (2011), that, for instance, the mass function of haloes would be significantly suppressed on mass scales $M \sim 100 M_{\rm fs}$.

In Fig. 1 we show the relation between $M_{\rm fs}$, $M_{\rm hm}$ and the mass of the WDM particle candidate for our adopted cosmological model. Three cases of relevance are apparent: $M > M_{\rm hm}$, and haloes form hierarchically through accreting material; $M_{\rm hm} > M > M_{\rm fs}$ and for these haloes the hierarchy may fail with low mass haloes forming at the same time as higher mass haloes; finally $M_{\rm fs} > M$ no halo formation, unless through the fragmentation of larger structures. While the growth of overdensities is not affected above $\rm M_{hm}$, it is suppressed between $\rm M_{fs}$ and $\rm M_{hm}$, and should simply not take place below $\rm M_{fs}$.

2.2 Nonlinear evolution of WDM: the halo model

Cosmological structure formation is a very complicated, highly nonlinear process that requires numerical simulation for a full understanding. However, the halo model approach gives a simplified analytical description of structure formation, which leads to surprisingly good results (Cooray & Sheth 2002, and references therein). Recently, the halo model has been adapted for the WDM cosmological model by Smith & Markovic (2011) and we now summarize their basic approach.

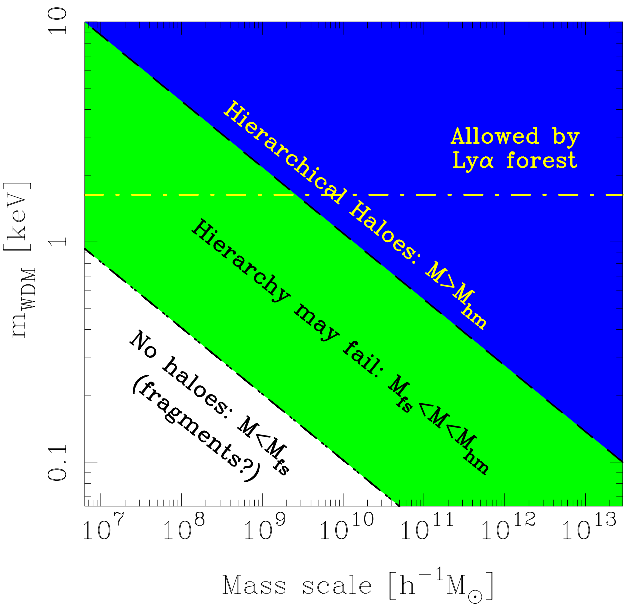

Figure 1. Free-streaming mass-scale ($M_{\rm fs}$) and half-mode mass scale ($M_{\rm hm}$) as a function of the mass of the WDM particle ($m_{\rm WDM}$). Haloes with masses $M > M_{\rm hm}$, may form hierarchically (upper right solid blue region). For haloes with masses $M_{\rm hm} > M > M_{\rm fs}$, hierarchical structure growth may fail (middle green region). For haloes with masses $M < M_{\rm fs}$, these may not form hierarchically since their initial peaks are completely erased (lower right empty region). However it is possible that such objects may emerge through fragmentation. The yellow dot-dash line denotes the current $m_{\rm WDM}$ allowed by the Lyman alpha forest (Boyarsky et al. 2009a) (note that we have rescaled $m_{\nu_s} \to m_{\rm WDM}$ using Eq. (6)).

The main idea of the halo model in WDM is to separate the density field into a halo component, adding up all bound structure, and a smooth component, standing for all matter, that has not collapsed due to free streaming. This is different to the standard approach of the CDM halo model, where all matter is supposed to be in bound structures.

Thus the WDM density field has the form,

$$\rho(\mathbf{x}) = \rho_s(\mathbf{x}) + \sum_{i=1}^{N} M_i u(|x - x_i|, M_i) , \tag{10}$$

where ρ_s is the smooth part of the density field and $u(x,M) = \rho_h(x|M)/M$ is the mass normalized density profile. The average densities of the smooth and the bound components are then given by

$$\langle\rho\rangle = \bar{\rho} = \bar{\rho}_{\rm s} + \bar{\rho}_{\rm h}, \qquad \bar{\rho}_{\rm h} = f\bar{\rho} , \tag{11}$$

where f is the fraction of matter in bound objects. This can be calculated by integrating over the halo mass function weighted by halo mass:

$$f = \frac{1}{\bar{\rho}}\int_0^\infty d\log M\, M \frac{dn}{d\log M} , \tag{12}$$

where $dn = n(M)dM$ is the abundance of WDM haloes of mass M in the interval dM. The fraction f is equal to unity in a perfectly hierarchical universe and drops below unity as soon as the mass function is suppressed due to the free streaming. In a WDM universe the amount of suppression depends on the mass of the WDM particle.

The power spectrum $P(k)$ is defined by the relation

$$\langle\delta(\mathbf{k})\delta(\mathbf{k}')\rangle \equiv (2\pi)^3\delta_D(\mathbf{k}+\mathbf{k}')P(k)\ , \tag{13}$$

where δ_D is the three dimensional Dirac delta function and $\delta(k)$ is the Fourier transform of the matter overdensity $\delta(\mathbf{x}) \equiv (\rho(\mathbf{x}) - \overline{\rho})/\overline{\rho}$. In terms of the different density components, we can write:

$$\delta(k) = f\delta_{\rm h}(k) + (1-f)\delta_{\rm s}(k), \tag{14}$$

where $\delta_\chi \equiv (\rho_\chi - \overline{\rho}_\chi)/\overline{\rho}_\chi$ with $\chi \in \{{\rm h},{\rm s}\}$. The power spectrum of the halo model can now be determined by adding up the power spectra of the different density components as well as their cross terms, giving

$$P(k) = (1-f)^2P_{\rm ss}(k) + 2(1-f)fP_{\rm sh}(k) + f^2P_{\rm hh}(k)\ . \tag{15}$$

The term $P_{\rm hh}$ represents the power spectrum of matter trapped in haloes, the term $P_{\rm ss}$ designates the power spectrum of the smooth component and the term $P_{\rm sh}$ denotes the cross-power spectrum between haloes and the smooth field.

The term $P_{\rm hh}$ can be separated into one- and two-halo terms, which describe the power coming from the same halo, and the one coming from distinct haloes, respectively. It can be expressed as:

$$P_{\rm hh}(k) = P_{\rm hh}^{\rm 2h}(k) + P_{\rm hh}^{\rm 1h}(k)\ ; \tag{16}$$

$$P_{\rm hh}^{\rm 2h}(k) = \prod_{i=1}^{2}\left\{\int_0^\infty \frac{dM_i}{\bar{\rho}_{\rm h}} M_i n(M_i) u(M_i)\right\} \times P_{\rm hh}^{\rm c}(k|M_1,M_2), \tag{17}$$

$$P_{\rm hh}^{\rm 1h}(k) = \frac{1}{\bar{\rho}_{\rm h}^2}\int_0^\infty dM n(M) M^2 u^2(k|M)\ , \tag{18}$$

where $u(k|M)$ is the Fourier transform of the mass normalized density profile. In Eq. (17) we have introduced the power spectrum of halo centers $P_c^{\rm hh}(k|M_1,M_2)$, which in general is a complicated function of k and the halo masses M_1 and M_2. However, if we neglect halo exclusion and assume linear biasing with respect to the linear mass density, then we may write this as,

$$P_{\rm hh}^{\rm c}(k|M_1,M_2) \sim b_1(M_1)b_1(M_2)P_{\rm lin}(k)\ . \tag{19}$$

In this case, the function is separable and this considerably simplifies the integrals in Eq. (17). This approximation breaks down on small, nonlinear scales, but on these scales, the two-halo term is sub-dominant. The error induced by this approximation (19) is most apparent at quasi-linear scales ($k \sim [0.1, 1.0]\,h\,{\rm Mpc}^{-1}$) and is $\lesssim 30\%$. It is possible to lower this error to $\lesssim 5\%$ by using higher order perturbation theory techniques and by including halo exclusion (see for example Smith et al. 2011). An easy but not fully consistent way of reducing the error down to $\lesssim 10\%$ is to do the following replacement in Equation (19):

$$P_{\rm lin}(k) \rightarrow P_{\rm halofit}(k)W_{\rm TH}(kR), \qquad R \simeq 2\,h^{-1}{\rm Mpc}, \tag{20}$$

where $W_{\rm TH}$ is the window function defined in §4.1 and $P_{\rm halofit}$ is the power spectrum calculated by the `halofit` code (Smith et al. 2003).

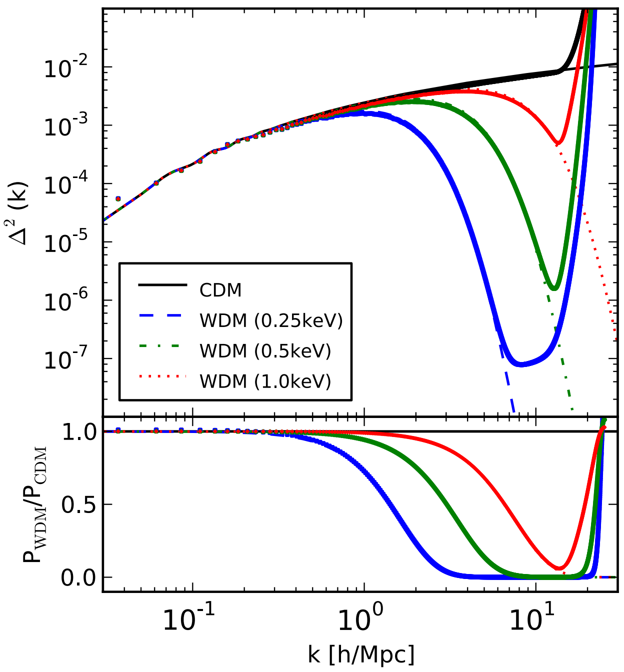

Figure 2. Linear power spectra as a function of wavenumber in the CDM and WDM scenarios, at the initial redshift ($z = 49$) of the simulations. *Top panel*: absolute dimensionless power: $\Delta^2 = k^3P(k)/2\pi^2$. The lines denote the linear power spectrum where $m_{\rm WDM} \in \{\infty, 0.25, 0.5, 1.0\}$ keV. Points denote the power spectra measured from the initial conditions of the $N = 1024^3$ simulations. *Bottom panel*: ratio of the initial WDM and CDM power spectra. Points and lines unchanged.

The halo-smooth power spectrum is given by:

$$P_{\rm sh}(k) = \frac{1}{\bar{\rho}_{\rm h}}\int dM n(M) M u(k|M) P_{\rm hs}^{\rm c}(k|M)\ , \tag{21}$$

where $P_{\rm hs}^{\rm c}(k|M)$ is the power spectrum of the halo centers with respect to the smooth mass field. On assuming that the smooth field and the halo density field are linearly biased with respect to the linear density field, we are lead to the relation:

$$P_{\rm sh}^{\rm c}(k|M) \sim b_s b(M) P_{\rm lin}(k)\ , \tag{22}$$

where b_s is the linear bias of the smooth matter field defined in §4.3. Finally, the smooth field auto-power spectrum is given by

$$P_{\rm ss}(k) = b_s^2 P_{\rm lin}(k)\ . \tag{23}$$

In order to reduce the error we can again replace the linear power spectrum in the Equations (22) and (23), following the recipe of relation (20).

On combining these power spectra, weighted by the correct functions of their mass fractions, à la Eq. (15), we find the total halo model prediction for the nonlinear matter power spectrum in the WDM model.

Sim label	$m_{\rm WDM}$ [keV]	$M_{\rm fs}\,[h^{-1}M_{\odot}]$	$M_{\rm hm}[h^{-1}M_{\odot}]$	$L\,[h^{-1}{\rm Mpc}]$	$N_{\rm part}$	$m_p\,[h^{-1}M_{\odot}]$	$l_{\rm soft}[\,h^{-1}{\rm kpc}]$
CDM-S	∞	0	0	256	256^3	7.57×10^{10}	20
CDM-M					512^3	9.45×10^{9}	10
CDM-L					1024^3	1.18×10^{9}	5
WDM-1.25-S	1.25	2.3×10^{6}	6.3×10^{9}	256	256^3	7.57×10^{10}	20
WDM-1.25-M					512^3	9.45×10^{9}	10
WDM-1.25-L					1024^3	1.18×10^{9}	5
WDM-1.0-S	1.0	4.9×10^{6}	1.3×10^{10}	256	256^3	7.57×10^{10}	20
WDM-1.0-M					512^3	9.45×10^{9}	10
WDM-1.0-L					1024^3	1.18×10^{9}	5
WDM-0.75-S	0.75	1.3×10^{7}	3.4×10^{10}	256	256^3	7.57×10^{10}	20
WDM-0.75-M					512^3	9.45×10^{9}	10
WDM-0.75-L					1024^3	1.18×10^{9}	5
WDM-0.5-S	0.5	4.9×10^{7}	1.3×10^{11}	256	256^3	7.57×10^{10}	20
WDM-0.5-M					512^3	9.45×10^{9}	10
WDM-0.5-L					1024^3	1.18×10^{9}	5
WDM-0.25-S	0.25	5.0×10^{8}	1.3×10^{12}	256	256^3	7.57×10^{10}	20
WDM-0.25-M					512^3	9.45×10^{9}	10
WDM-0.25-L					1024^3	1.18×10^{9}	5

Table 1. WDM simulations. From left to right, columns are: simulation name (S=Small, M=Medium, L=Large); mass of WDM particle ($m_{\rm WDM}$); free-streaming mass-scale ($M_{\rm fs}$); half-mode mass-scale ($M_{\rm hm}$); simulation box-size (L); number of particles ($N_{\rm part}$); mass of simulation particles ($m_{\rm p}$); comoving softening length ($l_{\rm soft}$).

3 N-BODY SIMULATIONS OF WDM

In order to study nonlinear structure growth in the WDM model, we have generated a suite of N-body simulations. These were executed on the `zBOX3` supercomputer at the University of Zürich. Each simulation was performed using `PKDGRAV`, a high order multipole tree-code with adaptive time stepping (Stadel 2001).

The cosmological parameters of the base ΛCDM model adopted, are consistent with the WMAP7 best-fit parameters (Komatsu et al. 2011) and we take: the energy-density parameters in matter, vacuum energy and baryons to be $\Omega_{\rm m}=0.2726$, $\Omega_{\Lambda}=0.7274$, $\Omega_{\rm b}=0.046$; the dimensionless Hubble parameter to be $h=0.704$; the primordial power spectral index and present day normalization of fluctuations to be $n_s=0.963$, and $\sigma_8=0.809$.

The CDM transfer function was generated using the code `CAMB` (Lewis et al. 2000). The linear power spectrum for each WDM model was then obtained by multiplying the linear CDM power spectrum by $T^2_{\rm WDM}(k)$ from Eq. (4). Initial conditions for each WDM model were then generated at redshift $z=49$ using the serial version of the publicly available `2LPT` code (Scoccimarro 1998; Crocce et al. 2006). In theory, we should also include a velocity dispersion due to the fact that the particles still retain a relic thermal velocity distribution. However, a quick calculation of the rms dispersion velocity, showed that these effects should be of marginal importance on scales $\gtrsim 50\,h^{-1}$kpc at the initial redshift, and of order $\gtrsim 1\,h^{-1}$kpc at the present day for $m_{\rm WDM}\geqslant 0.25\,[{\rm keV}]$. We therefore assume that their inclusion will be a second order effect and so at this stage we neglect them.

We generated initial conditions for a suite of simulations, one with a CDM particle and five with WDM particle masses $m_{\rm WDM}\in\{0.25,0.5,0.75,1.0,1.25\}$keV. For all runs, we set the box length $L=256\,h^{-1}$Mpc. This size is a compromise between choosing a box small enough to accurately capture small-scale structure formation and large enough to confidently follow the linear evolution of the box-scale modes. This makes it possible for us to check agreement with the linear theory and to measure linear bias.

Our simulations were also performed with three different mass resolutions: $N=\{256^3,\,512^3,\,1024^3\}$. This enables us to differentiate between genuine structures and spurious structures, which can collapse out of the initial particle lattice (cf. Wang & White 2007; Polisensky & Ricotti 2010). Full details of the suite of simulations are summarized in Table 1.

Dark matter haloes in the simulations were located using the Friends-of-Friends algorithm (Davis et al. 1985). We used a modified version of the `skid` code, with the linking length parameter set to the conventional value of $b=0.2$.

Fig. 2 compares the initial linear theory power spectra with the power spectra estimated from the initial conditions of the N-body simulations, for the case $N=1024^3$. These results show that, at the initial time, the WDM linear theory distribution of fluctuations has been correctly seeded. It also shows a spike in the measured power spectrum at $k=8\pi$ which is a consequence of the initial particle distribution on a grid.

Fig. 3 presents a pictorial view of the growth of structure in a selection of the simulations. The left column shows the density evolution in a slice through one of the CDM simulations. The central and right panels show the same but for the case of WDM particles with $m_{\rm WDM}=1.0\,$keV and $m_{\rm WDM}=0.25\,$keV. From top to bottom the panels show results for $z=4.4$, 1.1 and 0.

4 HALO MODEL INGREDIENTS IN THE WDM SCENARIO

In this section we detail the halo model ingredients and show how they change in the presence of our benchmark set of WDM particle masses.

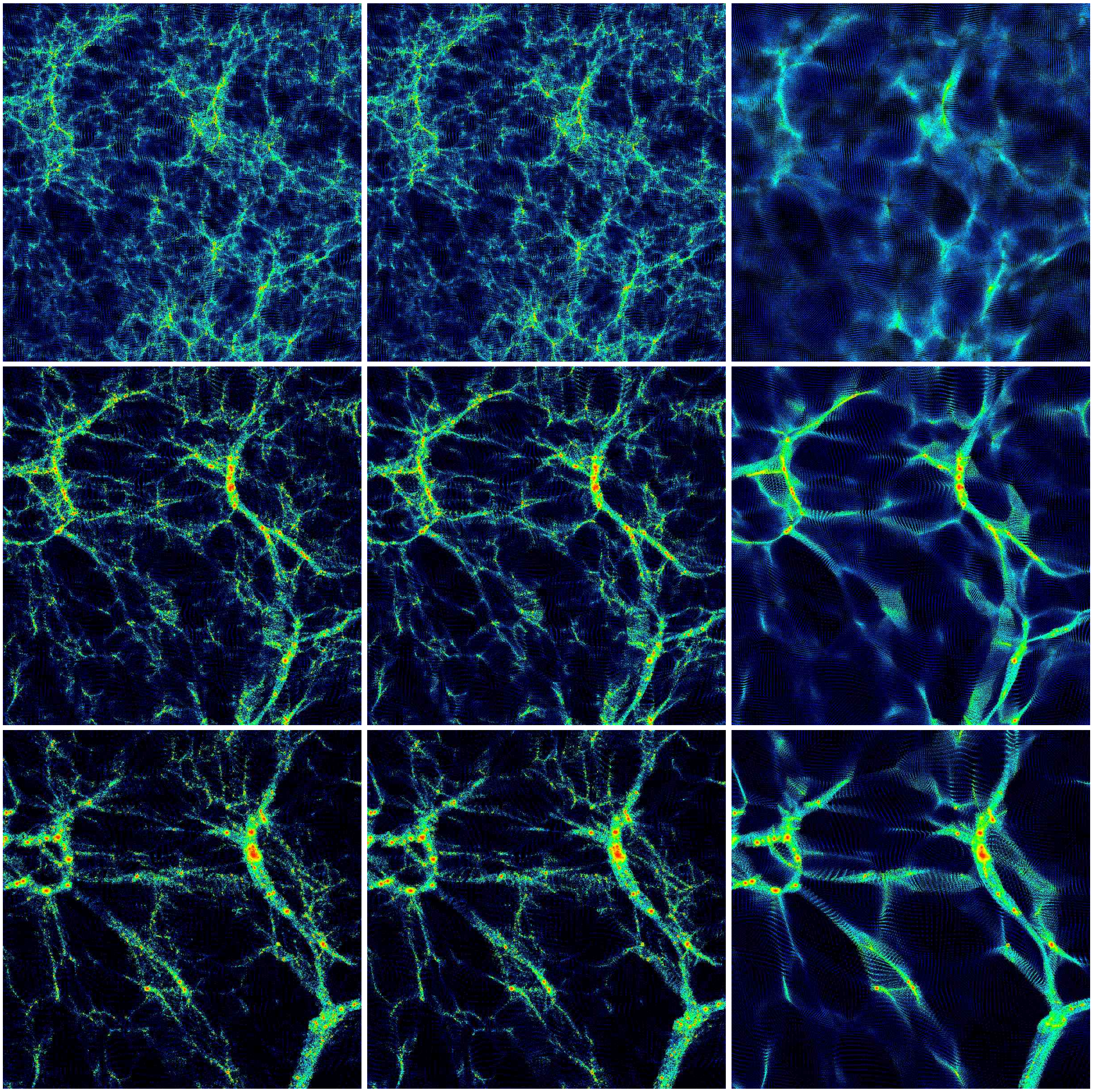

Figure 3. Density maps from the $N = 1024$ simulations with a length of $50\,h^{-1}$Mpc and a depth of $2.5\,h^{-1}$Mpc. From top to bottom: $z = 4.4$, $z = 1.1$ and $z = 0$. From left to right: CDM, WDM with $m_{\rm p} = 1.0$keV and WDM with $m_{\rm p} = 0.25$keV. Whilst the WDM effects are barely discernible in the middle panels, they are very prominent in the right panels, where the voids are noticeably emptier than in CDM.

4.1 Halo mass function

In CDM the halo mass function can be explored through the excursion set formalism (Press & Schechter 1974; Bond et al. 1991):

$$\frac{dn}{d\log M} = -\frac{1}{2}\frac{\bar{\rho}}{M} f(\nu) \frac{d\log\sigma^2}{d\log M}\ . \tag{24}$$

In the ellipsoidal collapse model of Sheth & Tormen (1999), $f(\nu)$ is given by

$$f(\nu) = A\sqrt{\frac{2q\nu}{\pi}}\left[1 + (q\nu)^{-p}\right] e^{-q\nu/2}, \quad \nu = \frac{\delta_c^2(t)}{\sigma^2(M)}, \tag{25}$$

with parameters: $p = 0.3$, $q = 0.707$ and with normalization parameter $A = 0.3222$. The linear theory collapse threshold is given by, $\delta_c(z) \equiv 1.686/D(z)$, where $D(z)$ is the linear theory growth function. The variance on mass scale M is,

$$\sigma^2(M) = \int \frac{{\rm d}^3\mathbf{k}}{(2\pi)^3} P_{\rm Lin}(k) W_{\rm TH}^2(kR)\ , \tag{26}$$

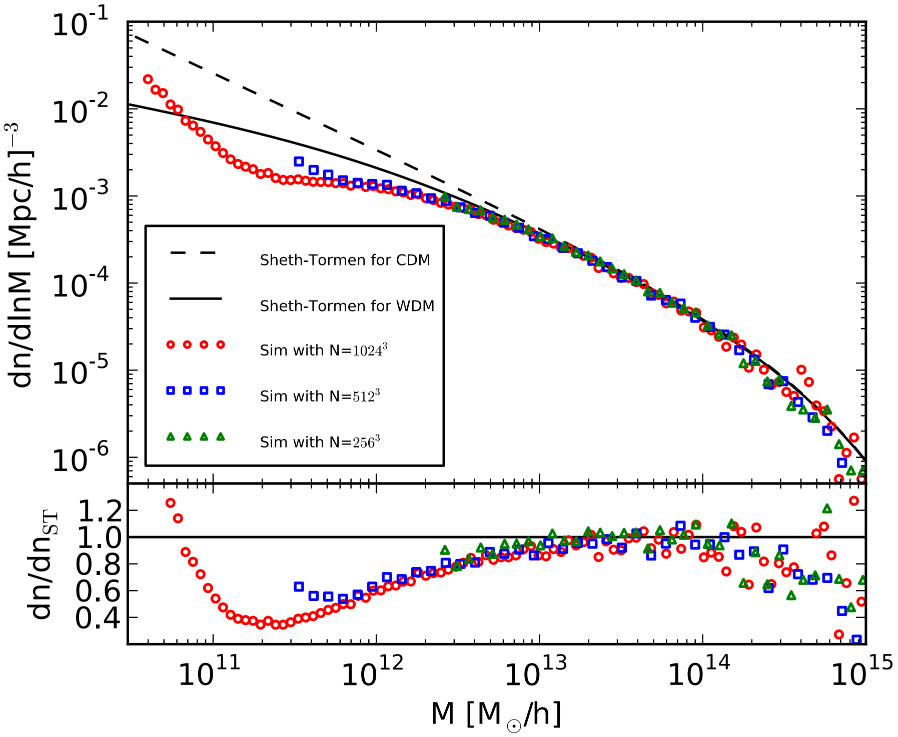

Figure 4. Measured mass function of the WDM simulations with $m_p = 0.25$ keV and three different resolutions. The measurements lie below the Sheth-Tormen prediction, a well known result that is discussed in section 4. The upturn of the mass function due to artificial haloes is visible in the simulations of high and medium resolution.

where $W_{\rm TH}(y) \equiv 3\left[\sin y - y\cos y\right]/y^3$ and where the mass scale and radius of the filter function are related through the relation: $M = 4\pi R^3\bar{\rho}/3$.

The main idea in the excursion set approach is that there is a monotonic mapping between the linear and nonlinear density perturbations, averaged over a randomly selected patch of points in the space. Further, the mapping can be calculated using the spherical or ellipsoidal collapse approaches. The density perturbation in the patch will collapse to form a virialized object when the linearly extrapolated density in the patch reaches a certain collapse threshold. Despite the fact that this approach does not trace the full complexity of nonlinear structure formation, the actual predictions are in close agreement with measurements from simulations. That is, at least for a CDM cosmology with well calibrated values for the ellipsoidal parameters p and q and a given halo finding algorithm. One important assumption, which is implicit within this framework, is that structure formation must proceed hierarchically.

In the WDM scenario, things are more complicated, since structure formation may not always proceed hierarchically. As described in §2, we can identify three regimes of interest: for $M > M_{\rm hm}$, the variance of WDM fluctuations becomes virtually indistinguishable from that for CDM, and the excursion set approach should be valid; for $M < M_{\rm fs}$ all primordial overdensities are erased through diffusion of particles during the epoch of radiation domination and we expect that no hierarchical halo formation will take place on these mass scales. In between, where $M_{\rm hm} > M > M_{\rm fs}$, the WDM overdensity field is suppressed, but there is still some power left that may enable hierarchical collapse to take place. It is not clear *a priori*, how the mass function behaves on these scales and whether the extended Press-Schechter approach remains valid. We now investigate this using our simulations.

In Fig. 4 we show the $z = 0$ mass function of dark matter haloes for the case of $m_{\rm WDM} = 0.25$keV. The figure demonstrates the behaviour of the mass function as the simulation resolution is increased from $N = 256^3$, to 512^3, to 1024^3 particles, denoted by the triangles, squares and circles, respectively. We can now see the effect of artificial clumping (cf. discussion in §3), which is manifest as the upturn of the curves at the low mass end of the mass function. One common approach to dealing with this artificial clumping is to assume that the simulations can be trusted down to the mass-scale just above the up-turn. We also find, in agreement with Wang & White (2007), that this mass-scale increases as $N^{1/3}$, i.e. the inter-particle spacing. In order to decrease the resolved mass by a factor of two, the particle resolution has to go up by a factor of eight. This is one of the main reasons why simulating WDM models is significantly more challenging than simulating CDM models.

Fig. 4 also shows the prediction of the halo mass function for CDM and for this WDM model, from the ST mass function. The figure clearly shows that the suppression of the ST model is not sufficiently strong to describe the data. In addition to this the ST mass function is diverging towards small masses, while we expect a realistic mass function to drop to zero at latest below the free streaming scale.

Fig. 5 compares the measurements of the WDM mass functions from a selection of our highest resolution simulations with the CDM case. We note that, whilst for the case

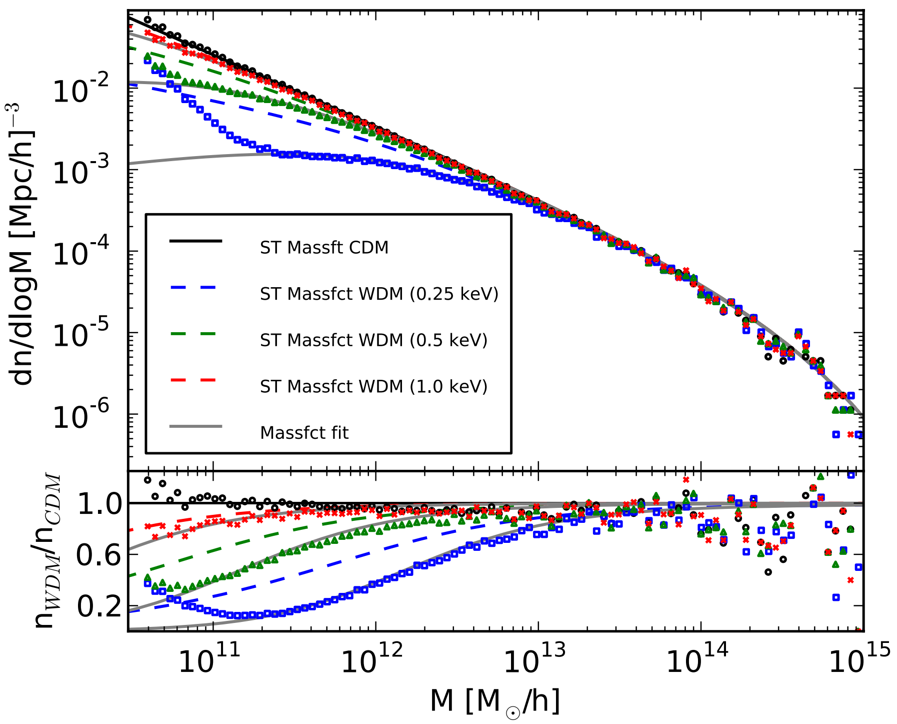

Figure 5. Comparison between the Sheth-Tormen mass functions (black solid line for CDM, colored dashed lines for WDM) and the measurements from the simulations (black circles for CDM, colored squares, triangles and crosses for WDM). The grey solid lines correspond to the mass function fit of Eq. (27).

of CDM the ST model is in very good agreement with the data, the WDM data all lie below the Sheth-Tormen prediction. That is, at least in the mass range above the artificial upturn of the mass function.

Currently, there is no theoretical model that can explain the discrepancy between the CDM and WDM measurements. We shall leave this as an issue for future study. However, it is possible to develop a fitting function that can describe the simulation results to high accuracy. As first noted in Smith & Markovic (2011), if one rescales the mass variable by $M_{\rm fs}$, or equivalently by $M_{\rm hm}$ (cf. §2), then the mass functions for a wide variety of different values of $m_{\rm WDM}$ all appear to fall upon the same locus[4].

In Fig. 6 we show that this scaling also works surprisingly well for the mass function measured from the simulations. We therefore look to fitting the rescaled mass functions. After trying various forms, we found that the function

$$\frac{n^{\rm A}_{\rm WDM}(M)}{n^{\rm ST}_{\rm WDM}(M)} = (1 + M_{\rm hm}/M)^{-\alpha}\,, \tag{27}$$

which has only one free parameter $\alpha = 0.6$ was able to fit all of our data with an rms error well below five percent.

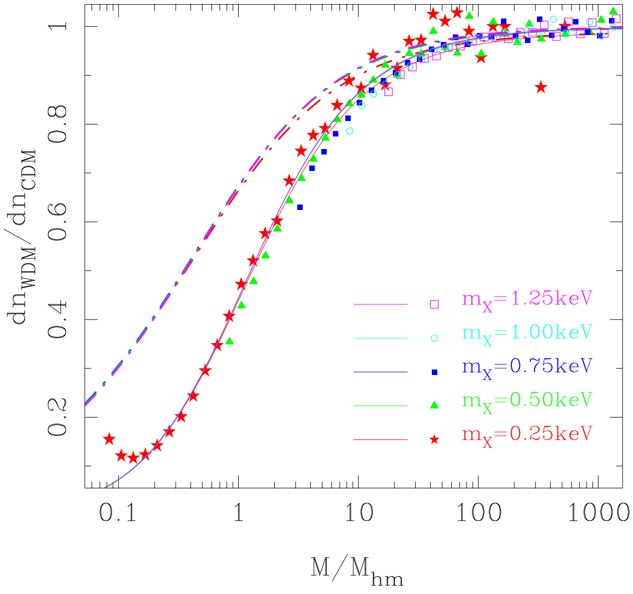

Figure 6. Ratio between the WDM and CDM mass functions, as a function of halo mass, scaled in units of the half-mode mass-scale $M_{\rm hm}$. The measurements from the $N = 1024^3$ suite of WDM simulations are denoted by the point symbols. The dot-dashed lines denote the predictions from the Sheth & Tormen (1999) CDM mass function applied to WDM. The solid lines show the results from the fitting formula of Eq. (27).

---

[4] We find that the locus of theory curves is much tighter than was first noted in Smith & Markovic (2011). This owes to the fact that, they adopted the free-streaming scale of Bardeen et al. (1986); Zentner & Bullock (2003), but used the transfer function of Viel et al. (2005) to generate the actual linear theory power spectra. This slight mismatch led to a slight off-set, which as Fig. 6 shows, is removed when consistent definitions for $M_{\rm fs}$ and $M_{\rm hm}$ are adopted.

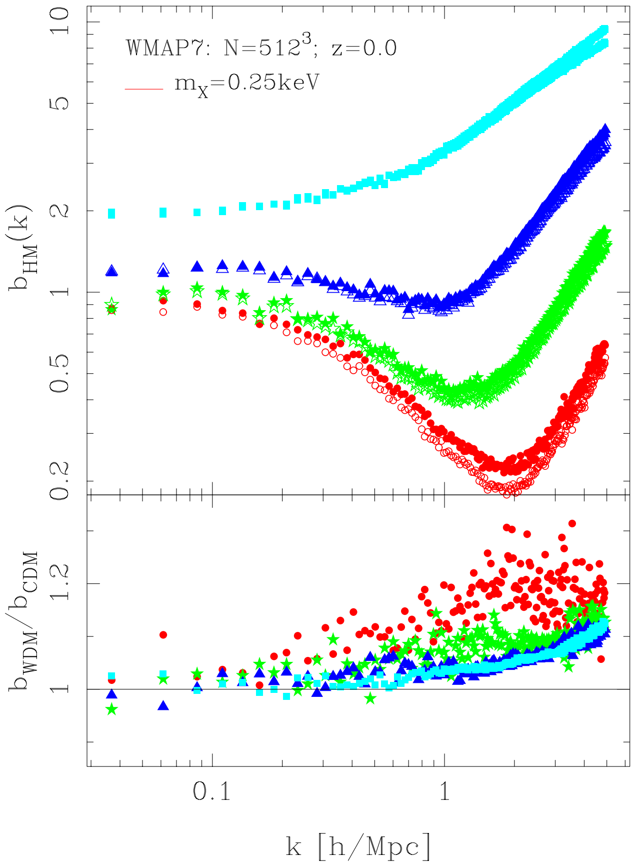

Figure 7. *Top panel*: Comparison of halo bias in the CDM and $m_{\rm WDM} = 0.25$keV WDM model, as a function of wave number. The open and solid points denote the results for CDM and WDM, respectively. Circles, stars, triangles and squares denote results for haloes with masses in the range: $\log_{10}\left(M/[h^{-1}M_\odot]\right) \in \{[12.0, 12.5], [12.5, 13.0], [13.0, 13.5][>13.5]\}$ *Lower panel:* Ratio of the bias in the WDM model with that for the CDM model. For $k > 0.1\,h\,{\rm Mpc}^{-1}$ we see a relative excess signal in the bias of haloes with $M > 10^{12}h^{-1}M_\odot$ in the WDM models. For $k < 0.1\,h\,{\rm Mpc}^{-1}$ the trends are unclear owing to sample variance.

Note that in the above, $n^{\rm ST}_{\rm WDM}$ is the Sheth-Tormen model evaluated for the WDM model in question. The resulting mass functions are plotted as the grey solid lines in Fig. 5. A slightly worse fit may be obtained by using the function,

$$\frac{n^{\rm B}_{\rm WDM}(M)}{n_{\rm CDM}(M)} = (1 + M_{\rm hm}/M)^{-\beta} \,, \tag{28}$$

with $\beta = 1.16$ and this has the advantage that, one only needs to evaluate the CDM mass function and rescale the masses. We note that whilst this paper was being prepared, a similar study was presented by Dunstan et al. (2011), who showed that $n^{\rm B}_{\rm WDM}$ provided a good description of their data but with the slightly higher value $\beta = 1.2$.

Finally, we examined the evolution of the WDM mass-functions up to $z = 1$ and found that Eq. (27) also provides a good description of this data. The simplicity and generality of the fitting function Eq. (27) is surprising and we think that it will be a useful empirical formula.

4.2 Halo bias

We are also interested in understanding how the density fields of dark matter haloes and matter are related in the WDM framework. This relation is usually termed bias, and if we assume that bias is local, deterministic, and linear, then we may write:

$$\delta_{\rm h}({\bf x}|M) = b(M)\delta_{\rm m}({\bf x}) \,, \tag{29}$$

where $b(M)$ is the linear bias coefficient, which depends only on the mass of the halo. On using the excursion set formalism and the peak background split argument, one may obtain a prediction for $b(M)$ (Cole & Kaiser 1989; Mo & White 1996; Sheth & Tormen 1999):

$$b^{\rm ST}(\nu) = 1 + \frac{q\nu - 1}{\delta_c(z)} + \frac{2p}{\delta_c(z)\,[1 + (q\nu)^p]} \,, \tag{30}$$

where the parameters p and q are as in Eq. (25). As was shown in Smith & Markovic (2011), if we apply this formula to the case of WDM, then we would expect to see that for $M > M_{\rm hm}$ the bias function is identical to that obtained for CDM. However, for $M < M_{\rm hm}$ we expect to find that the halo bias is increased relative to the CDM case. This occurs due to the fact that ν tends towards a constant value for $M < M_{\rm hm}$ and so $b^{\rm ST}$ becomes constant as well. We again use the simulations to investigate these predictions.

In order to estimate the halo bias, we first sliced the halo distribution into a set of equal number density mass bins. Then, for each mass bin, we estimate the halo and matter auto-power spectra $P^{\rm hh}(k|M)$ and $P^{\rm mm}(k)$, respectively. Our estimator for the bias at each k-mode and in mass bin M_α, can be written:

$$b_i(k_i, M_\alpha) \equiv \sqrt{\frac{P^{\rm hh}(k_i|M_\alpha) - 1/n_{\rm h}(M_\alpha)}{P^{\rm mm}(k_i)}} \,, \tag{31}$$

where $n_{\rm h}(M_\alpha)$ is the number density of haloes for the mass bin α.

Fig. 7 compares the scale-dependence of the halo bias, for several mass bins, and as a function of the wavemode, for the case of CDM (open points) and for the $m_{\rm WDM} = 0.25$ keV WDM model (solid points). Note that here we actually present $b^{\rm hm}(k) \equiv P^{\rm hm}/P^{\rm mm}$, where $P^{\rm hm}$ is defined by the relation $(2\pi)^3\delta_{\rm D}({\bf k}+{\bf k}')P^{\rm hm} = \langle\delta_{\rm h}({\bf k})\delta_{\rm m}({\bf k}')\rangle$. In examining the ratio $b_{\rm WDM}/b_{\rm CDM}$, we see that there is increased bias in the WDM case.

We then combine the estimates from each Fourier scale using a standard inverse variance weighted estimator (see e.g. Smith et al. 2007). Also, since, in this case, we are mainly interested in determining the effective linear bias, we only include modes with $k < 0.1\,h\,{\rm Mpc}^{-1}$ (cf. Fig. 7). Fig. 8 presents the linear bias measurements together with the predictions from $b^{\rm ST}(M)$ for a selection of the simulated WDM models. The four panels show the cases: CDM, top left; $m_{\rm WDM} = 1.0$keV, top right; $m_{\rm WDM} = 0.5$keV, bottom left; $m_{\rm WDM} = 0.25$keV, bottom right.

Considering the high mass haloes, we find that the bias estimates for CDM and the WDM models appear to be in reasonable agreement with one another. At lower masses, however, there is a prominent increase in the bias for the WDM models with the lightest particle masses. We have found that, rather than a genuine effect due to WDM initial conditions, this boost appears to be a manifestation of

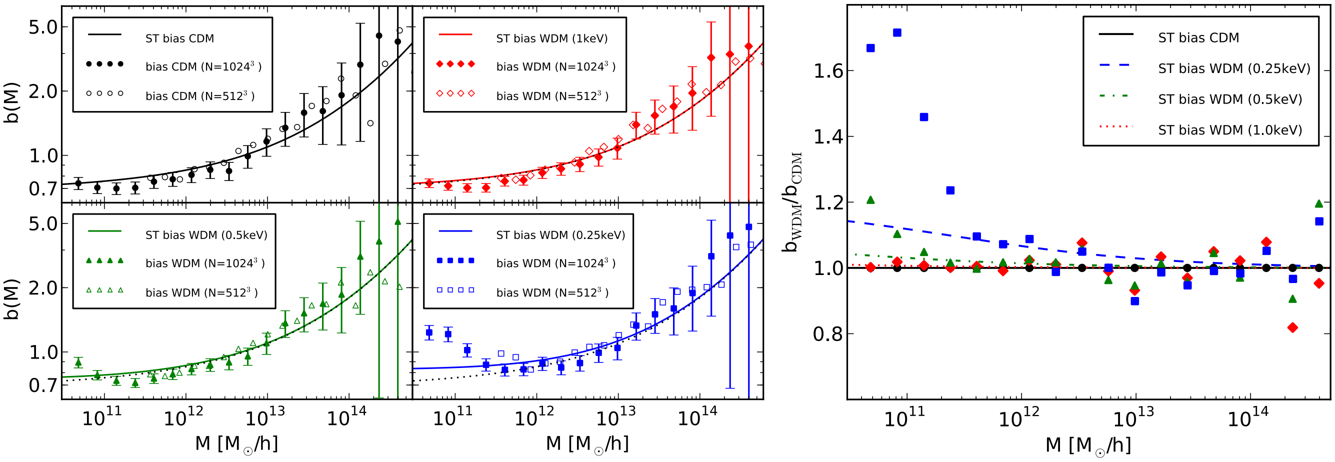

Figure 8. Left panel: Linear halo bias for CDM (top left) and WDM (top right: 1.0 keV, bottom left: 0.5 keV and bottom right: 0.25 keV). The filled and empty dots are measurements from the simulations with $N = 1024^3$ and $N = 512^3$, respectively. Error bars are calculated with an inverse variance wieghted estimator (see Smith et al. 2007). The solid lines correspond to the Sheth-Tormen model prediction of Eq. (30). The linear halo bias of CDM is shown as a black dotted line for comparison. Right panel: Ratios between the WDM and the CDM linear halo bias for the $N = 1024^3$ runs. The error bars have been omitted for clarity.

the artificial halo clumping discussed in §3. This becomes obvious by looking at the bottom-right plot in the panel on the left of Fig. 8, where the upturn of the high resolution simulation (solid blue squares) is shifted with respect to the upturn in the low resolution simulation (empty blue squares). The mass scales of the upturn in the halo bias coincides with the upturn in the mass function (see Fig. 4). Importantly, this means that the halo-halo power spectrum is strongly contaminated by the spurious haloes, even on scales that are considered to be linear. To some extent this is not so surprising, given that below a certain mass scale we are dominated by spurious clumps.

In general, when considering masses above the minimum mass-scale that we trust, rather than an excess bias with respect to $b^{\rm ST}$, we see that the estimates appear to lie slightly below the theoretical prediction at low masses. This has been observed in the CDM framework by Tinker et al. (2010), and it seems to be the case for both our CDM and WDM simulations. However, for the case of $m_{\rm WDM} = 0.25$, we do note that, just above the non-physical upturn, there is a sign that bias in the WDM simulations is larger than in the CDM case. This trend is in qualitative agreement with the Sheth-Tormen prediction for WDM. However, the effect is small and of the order of the error bars and one would need both larger volume and higher resolution simulations to robustly confirm this.

4.3 Anti-bias of the smooth component

We also require the density field of the smooth matter. As for the case of the halo bias, if we assume that this is a linear, deterministic function of the matter density, then we may write the simple expression:

$$\delta_{\rm s}(\mathbf{x}) = b_{\rm s}\delta(\mathbf{x}) \ , \tag{32}$$

where $b_{\rm s}$ is the smooth bias parameter. As shown in Smith & Markovic (2011), this can be calculated using a mass conservation argument, and one finds:

$$b_s = \frac{1}{1-f}\left[1 - \frac{1}{\bar{\rho}}\int dM M n(M) b_1(M)\right] \leqslant 1 \tag{33}$$

Unlike the halo bias, which is mass dependent, the linear bias of the smooth component stays constant over all scales. In consequence, the smooth component of the power spectrum is directly proportional to the linear matter power spectrum. We shall leave it for future study to establish the veracity of this expression.

4.4 Density profiles

Over the years, extensive numerical work has shown that, for the case of the CDM model, the density profiles of dark matter haloes are reasonably well characterized by the NFW profile (Navarro et al. 1997; Moore et al. 1999; Diemand et al. 2004; Springel et al. 2008; Stadel et al. 2009). This has the universal form:

$$\frac{\rho(r)}{\bar{\rho}} = \frac{\delta_{\rm s}}{y(1+y)^2} \ ; \qquad y \equiv \frac{r}{r_{\rm s}} \ , \tag{34}$$

where the two parameters $\delta_{\rm s}$ and $r_{\rm s}$ represent a characteristic overdensity and scale radius. The mass of each halo can be determined by simply summing up the number of particles in a given object and multiplying by the particle mass. We can connect this to the virial radius through the relation:

$$M_{\rm vir} = \frac{4\pi}{3}\bar{\rho}\Delta_{\rm vir}r_{\rm vir}^3, \tag{35}$$

where $r_{\rm vir}$ and $\Delta_{\rm vir}$ are the virial radius and overdensity, respectively. The value of $\Delta_{\rm vir}$ is typically chosen to denote the overdensity for virialization, and here we adopt the value $\Delta_{\rm vir} = 200$ (e.g. see Sheth & Tormen 1999). However, the halo mass $M_{\rm vir}$ can also be obtained by integrating the density profile up to $r_{\rm vir}$, which gives

$$M_{\rm vir} = 4\pi\bar{\rho}\delta_{\rm s}r_s^3\left[\log(1+c_{\rm vir}) - c_{\rm vir}/(1+c_{\rm vir})\right] \ , \tag{36}$$

where we have introduced the concentration parameter, defined as $c_{\rm vir} \equiv r_{\rm vir}/r_{\rm s}$. On equating Eqs (35) and (36) we find that

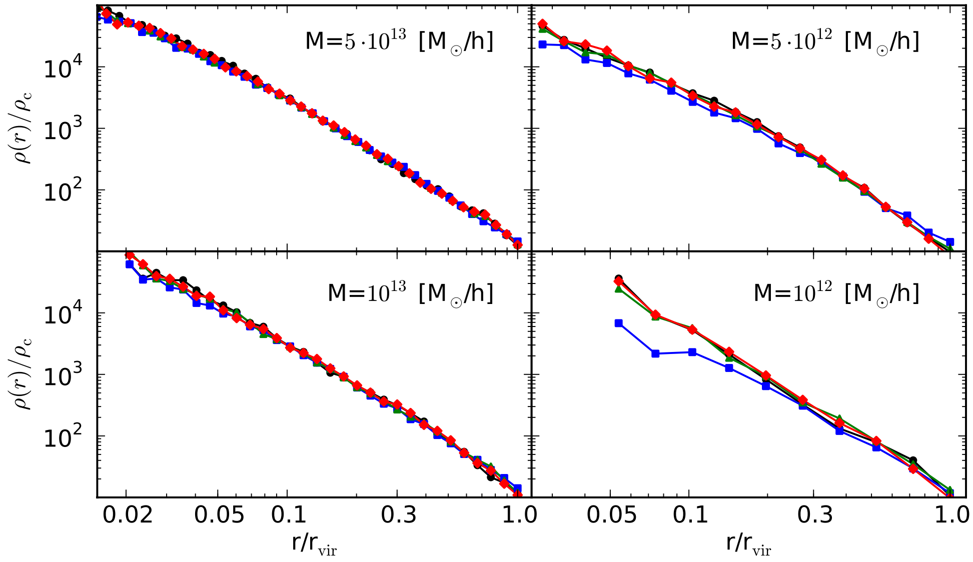

Figure 9. Measurement of the halo profiles for CDM (black) and WDM (blue: 0.25 keV, green: 0.5 keV, red: 1.0 keV) for different halo masses. The profiles of each mass bin are coming from a randomly chosen halo, which is identified in the CDM and all WDM simulations.

$$\delta_{\rm s} = \frac{c^3 \Delta_{\rm vir}/3}{[\log(1+c_{\rm vir}) - c_{\rm vir}/(1+c_{\rm vir})]} \; . \qquad (37)$$

This means that the original parameters $\{\delta_{\rm s}, r_{\rm s}\}$ of the NFW profile can be replaced by $\{M_{\rm vir}, c_{\rm vir}\}$. Thus, given a simulated halo of mass $M_{\rm vir}$, the model has one free parameter, the concentration parameter $c(M)$

Fig. 9 shows the density profiles of several randomly chosen haloes of different masses, for the case of CDM (black connected points). We have matched these objects with their counterpart haloes in the our standard set of WDM models and their profiles are also plotted (coloured connected points). While these profiles, on this logarithmic plot, all appear virtually indistinguishable for high masses, there does appear to be a net flattening off in the inner radius for the galaxy mass haloes in the WDM model with $m_{\rm WDM} = 0.25$keV. One important point that can not be easily gleaned from the figure, is that there is an overall reduction in the masses of all the smaller haloes. As we will see, this will have important consequences when we characterize the $c(M)$ relation in the next section.

Earlier work on this topic by Moore et al. (1999) found that there was almost no perceptible difference between CDM haloes and haloes that formed from CDM initial conditions that had no small scale power below a certain scale. Subsequent work by Avila-Reese et al. (2001) and Colín et al. (2008), with a more careful treatment of the WDM transfer function, have shown more significant differences. However, in this case they were exploring models that were closer to HDM than WDM. We therefore conclude that our results are broadly consistent with all of these findings.

One further point, is that for this small sample, we see no visible signs of the formation of a constant density core. This is in agreement with work Villaescusa-Navarro & Dalal (2011). Adding thermal velocities into the simulations could in principle lead to the formation of a constant density core through the Tremaine & Gunn (1979) limit on the fine grained phase space. However, the thermal velocities of WDM cool down with the expansion of space and are already very small during the epoch of structure formation. Thus, if cores are induced, we expect that they will lie below the resolution limit of our simulations (see Kuzio de Naray et al. 2010, for more discussion of this).

In summary, NFW profiles remain a valid approximation for density profiles in our WDM simulations, given our spatial resolution and choice of $m_{\rm WDM}$.

4.5 Concentration-mass relation

As shown in the previous section the NFW model can be fully characterized by specifying the concentration mass relation. We now explore this for the case of WDM.

In the CDM model, $c_{\rm vir}$ has been shown to be a monotonically decreasing function of $M_{\rm vir}$ (Navarro et al. 1997; Bullock et al. 2001; Macciò et al. 2007, 2008; Neto et al. 2007; Prada et al. 2011). One explanation for this, is that owing to the fact that haloes of different mass form at different times, they are therefore exposed to different background densities at collapse and this influences the final core overdensity. A denser background during collapse leads to generally higher concentrations. These ideas were encapsulated into a simple model for halo concentration by Bullock et al. (2001):

$$c_{\rm vir} = K(z_c+1)/(z+1) \; , \qquad (38)$$

where z_c is the redshift of collapse. This can be obtained by solving the relation $\sigma(M_*, z) = 1.686$, where $M_* \equiv F M_{\rm vir}$, is defined to be a constant fraction of the virial mass. The two constants K and F must be calibrated using numerical simulations, and for our CDM simulations we found that $K = 3.4$ and $F = 0.001$ provided a good fit to the data. However, we note that the above arguments are only qualitatively correct, since, as first pointed out by Bullock et al. (2001), there is a large scatter between $c_{\rm vir}$ and $M_{\rm vir}$. This can, in part, be traced to the varying accretion histories and large-scale environments of different haloes of the same final mass.

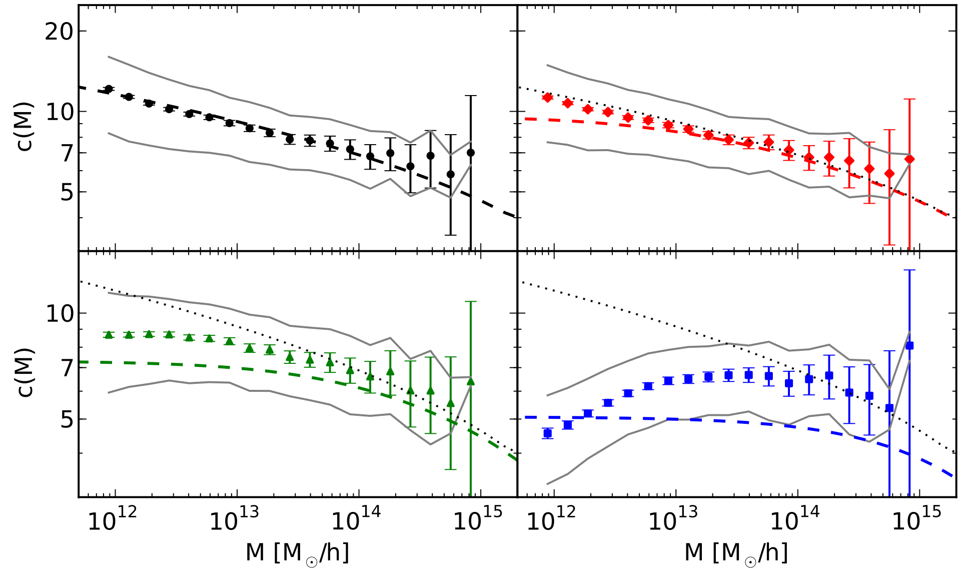

Figure 10. Concentration to mass relation for CDM (top left) and for WDM with $m = 1$ keV (top right), $m = 0.5$ keV (bottom left) and $m = 0.25$ keV (bottom right). The colored symbols denote the median concentrations, while the dashed lines correspond to the Bullock model with $F = 0.001$ and $K = 3.4$. For comparison the Bullock model for CDM has been added to the WDM plots in form of a black dotted line. The gray lines are the 1-σ contours.

Turning to the WDM case, if we directly apply the Bullock model, but using the WDM linear power spectrum, then we find a suppression and a flattening of halo concentrations for masses $M < M_{\rm hm}$. Similar to the mass function, this arises due to the fact that $\sigma(M)$ saturates to a constant value for masses approaching $M_{\rm fs}$. We have tested these predictions, by estimating the concentration parameters for all *relaxed* haloes in our CDM and WDM simulations that contain more than $N = 500$ particles (for full details of the method that we employ see Macciò et al. 2007, 2008).

Fig. 10 shows the measured halo concentrations as a function of mass for a selection of the highest resolution CDM and WDM simulations. The gray solid lines correspond to the 1-σ contours of the measurements, indicating a considerable spread in the concentration-mass relation. The large solid symbols denote the median, with the errors being computed on the mean, i.e. we use $\sigma/\sqrt{N_i}$, where N_i are the number of haloes in the ith mass bin. The dashed lines denote the predictions from the Bullock model. For the CDM case it works reasonably well, especially with our modified parameters $\{K, F\}$. However, the model shows the wrong qualitative behavior for the WDM scenario: whilst the curve for the Bullock model always flattens out towards low masses, we see that for the cases of the lighter WDM particles, there is a turnover in the relation. This turnover in the $c_{\rm vir}$–M relation at low masses is important, as it indicates the end of hierarchical collapse and the emergence of a period of top-down structure formation. As a test of these results we performed additional WDM runs with the `Gadget-2` gravity code (Springel 2008) and we observe the same turnover in this independent set of simulations.

In order to model the $c_{\rm vir}$–M relation for WDM, we shall adapt the Bullock model. As in the case of the mass function, we do this by introducing a correction function described by the relation:

$$\frac{c_{\rm WDM}(M)}{c_{\rm CDM}(M)} = \left(1 + \gamma_1 \frac{M_{\rm hm}}{M}\right)^{-\gamma_2} , \qquad (39)$$

where we have again rescaled the halo mass by $M_{\rm hm}$. Least-squares optimization of the free-parameters gives: $\gamma_1 = 15$ and $\gamma_2 = 0.3$.

In Fig. 11 we compare the fitting function (gray solid lines) with the results from the simulations. The parametric relation describes the $c_{\rm WDM}$–M relation with a precision of better than 10% (the fit appears less satisfying for the case $m_{\rm WDM} = 0.5$keV, but only for the lower mass bins). Interestingly, the value $\gamma_1 \sim 10$, informs us that the $c(M)$ relation is sensitive to the presence of WDM for mass scales one order of magnitude larger than for the mass function. As we will see in the next section, this will be important for modeling the nonlinear power spectrum on small scales.

5 NONLINEAR POWER SPECTRUM

5.1 Comparison with existing models

In Fig. 12 we show the nonlinear matter power spectra estimated from our highest resolution CDM and WDM simulations. One can see that for $k \leqslant 1\,h\,{\rm Mpc}^{-1}$, there appears to be no obvious difference between the CDM and WDM models under consideration. This is in stark contrast with the initial linear theory power spectra (cf. Fig. 2), which show considerable damping for the same scales. Clearly nonlinear evolution has regenerated a high-k tail to the power spectrum (cf. White & Croft 2000). At higher wavenumbers $k > 1\,h\,{\rm Mpc}^{-1}$, the situation is more interesting, and we see that the measured WDM power spectra are suppressed with respect to the CDM spectrum. The bottom panel of Fig. 13 quantifies this suppression in greater detail. Here we see that at $k \sim 10\,h\,{\rm Mpc}^{-1}$ there is a 20% suppression in power for the case of $m_{\rm WDM} = 0.25$keV and this drops to $\sim 2\%$ for

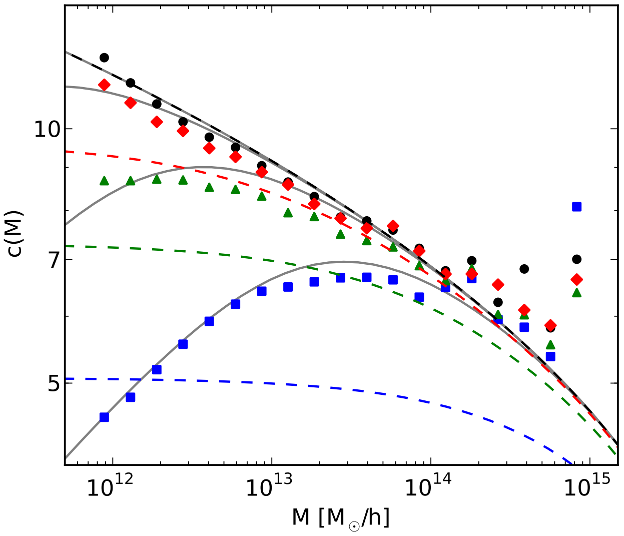

Figure 11. Same as Fig. 10 but measurements are superimposed on one another and without error bars. The additional gray lines illustrate the fitting function from Eq. (39).

the case $m_{\rm WDM} = 1$keV. The small difference between CDM and WDM at large scales ($k \lesssim 1$) is coming from a shift in the amplitude of the linear power spectrum, fixed with the same σ_8.

We now explore whether the halo model approach, described in §2.2, can accurately reproduce our results for the WDM power spectra. In the original WDM halo model calculation of Smith & Markovic (2011), all of the model ingredients (mass function, density profiles and halo bias relation), were obtained by assuming that the CDM relations also applied to the WDM case, provided one computes them using the appropriate linear power spectrum. The results of this approach are presented in Figs 12 and 13 as the coloured line styles.

In Fig. 13 we see that the halo model of Smith & Markovic (2011) under-predicts the WDM power spectra by roughly $\sim 10\%$. This is reasonably good, considering the assumptions that went into the model. This discrepancy was also noted in the study of Viel et al. (2011). In the bottom panel of Fig. 13 we have also compared our nonlinear power spectra with the predictions from the fitting formula presented in Viel et al. (2011). For scales $k < 10\,h\,{\rm Mpc}^{-1}$ we find that this fitting function provides an excellent description of our data. However, for $k > 10\,h\,{\rm Mpc}^{-1}$ we find discrepancies, especially for the case $m_{\rm WDM} = 0.25$keV. Whether this is a genuine failing of the fitting formula is not clear, since this scale coincides with $\sim k_{\rm Ny}/2$, where $k_{\rm Ny} = \pi N_{\rm grid}/L$ is the Nyquist frequency and we have used $N_{\rm grid} = 2048$.

In summary, we find that the original halo model overestimates the suppression of power due to WDM. This is not too surprising, since we have seen in the previous section that the original approximations for the halo mass function and concentrations turn out to be insufficient descriptions of the simulation data.

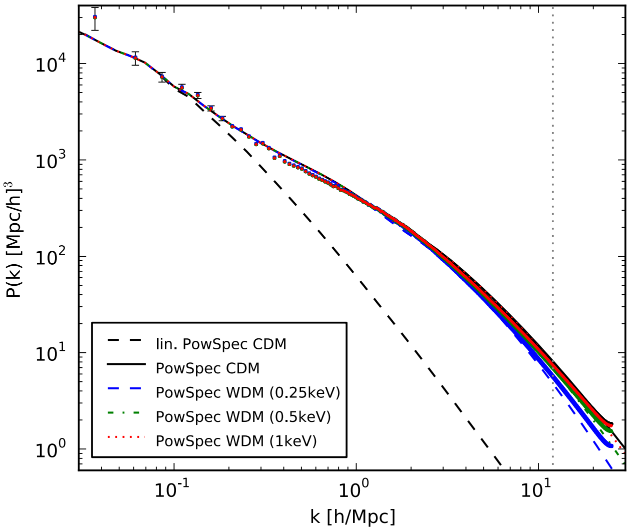

Figure 12. Nonlinear power spectra from the simulations (dots) and from the original halo model (lines), developed by Smith & Markovic (2011). Black corresponds to CDM and color to WDM (red: 1 keV, green: 0.5 keV, blue: 0.25 keV). The vertical gray dots indicate half the Nyquist frequency.

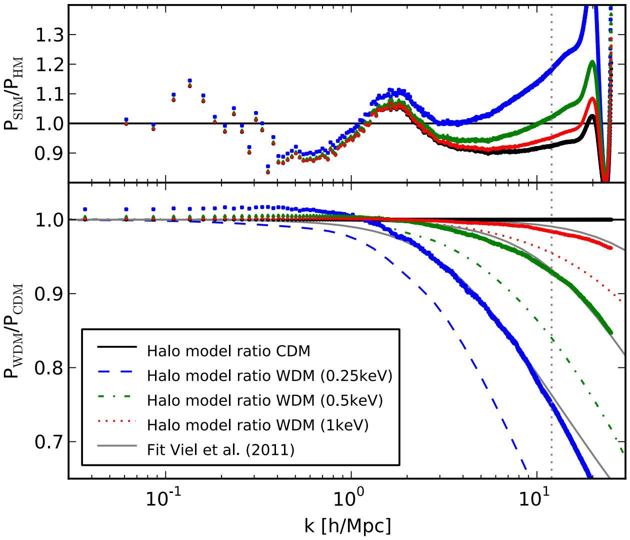

Figure 13. *Top panel*: Ratio of the simulated matter power spectra with respect to the halo model predictions as a function of wavenumber. Different coloured symbols denote the CDM and a selection of the WDM models. *Bottom panel:* Ratio of the WDM and CDM power spectra as a function of wavenumber. Points denote the results from the ratios of simulation data; lines denote the halo model results. The gray solid lines correspond the fitting function from Viel et al. (2011).

5.2 Towards an improved WDM halo model

We now explore whether the halo model predictions can be improved by employing our better fitting functions for $n(M)$ and $\rho(r|M)$. Before making a final prediction for $P(k)$, we first examine how each modification affects the predictions individually.

If we implement our correction for the WDM mass function in the $P(k)$ predictions, then, since the abundance of

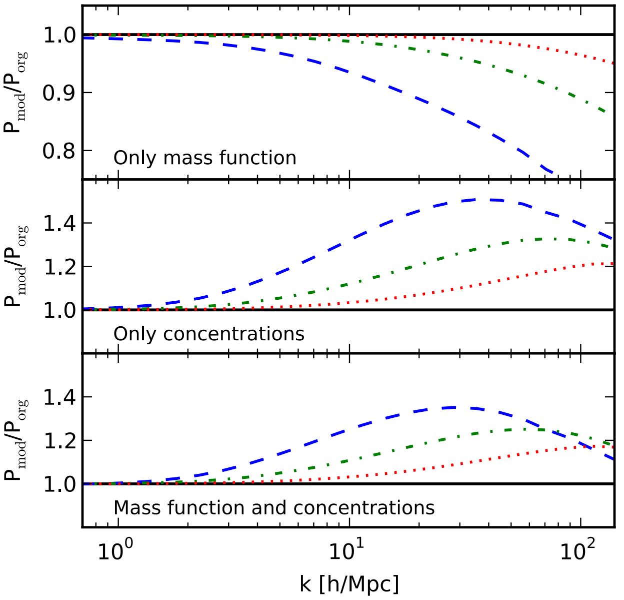

Figure 14. Ratio between modified versions of the halo model and the original version from Smith & Markovic (2011). The black solid line corresponds to CDM and the colored lines to WDM (red dotted: 1 keV, green dashed-dotted: 0.5 keV and blue dashed; 0.25 keV). Top panel: only modification of the mass function. Middle panel: only modification of the concentration-mass relation. Bottom panel: modification of mass function and concentration-mass relation.

small haloes is additionally suppressed with respect to the predictions of $n^{\rm ST}$ for WDM, we should expect that there is an even stronger suppression in $P(k)$. This conjecture is confirmed in the top panel of Fig. 14, which presents the ratio between the halo model with our modified mass function and the original one. We clearly see that the ratio always remains below unity. Somewhat surprisingly, we also note that a $\sim 50\%$ change in the abundance of $10^{12}h^{-1}M_\odot$ haloes, leads to a relatively small change, $\lesssim$ 10%, in the power spectrum at $k \lesssim 10\,h\,{\rm Mpc}^{-1}$.

Next, if we instead implement our improved $c_{\rm vir}(M)$ relation, then we find that this has a more significant impact on the spectra. The central panel of Fig. 14 shows the ratio between the halo model with the modified concentrations and the original one. We find that the suppression of the halo concentrations leads to a $\sim 50\%$ boost in the power for $k \sim 40\,h\,{\rm Mpc}^{-1}$.

The lower panel of Fig. 14 shows the combined behavior of both corrections. The ratio between the fully modified halo model and the original one remains larger than unity. Thus, combination of the modified $n(M)$ and $c(M)$, leads to halo model predictions that have relatively more small-scale power.

Finally, in Fig. 15 we present the comparison between our improved halo model and the nonlinear power spectra from the simulations. The top panel presents the ratios between the simulation data and the halo model predictions. The bottom panel shows the ratios of the WDM and CDM results for both the simulations and our modified halo model. Considering $k \gtrsim 3\,h\,{\rm Mpc}^{-1}$, whilst our modified halo model still has some problems predicting the overall absolute value of $P(k)$, the relative changes between the WDM models and CDM are almost exactly predicted, they being accurate to better than $\sim 2\%$ down to $k \sim 10\,h\,{\rm Mpc}^{-1}$. For scales beyond $k \gtrsim 10\,h\,{\rm Mpc}^{-1}$ we see that the halo model also matches the simulations very well. However, again we note that these scales are beyond $k_{\rm Ny}/2$ and so one might worry about aliasing effects. For $k \lesssim 3$ the error is below about 5%, this scales are however suffering from the difficulties in calculating $P^{\rm c}_{\rm hh}$, described in §2.2.

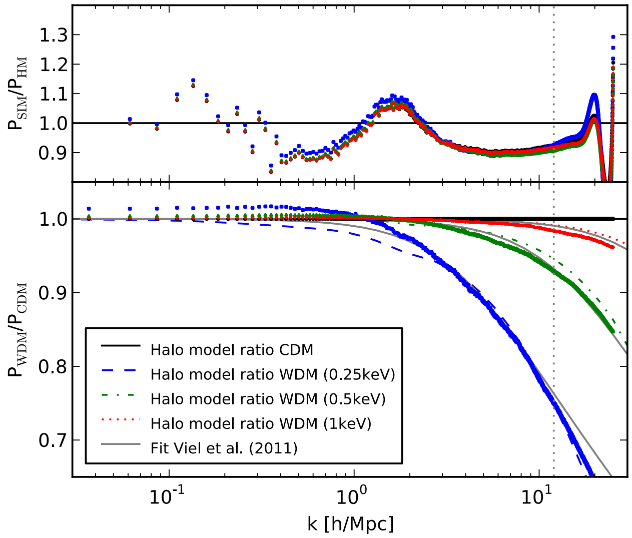

Figure 15. Nonlinear power spectra from the simulations (dots) and from the fully corrected halo model (lines), including the fits for the mass function and the concentrations. The labeling is the same than in Fig. 12. The error of the halo model compared to the simulations has dropped below 10 percent (top pannel), the error on the ratio between WDM and CDM has dropped well below 5 percent (bottom pannel).

In summary, we conclude that our modified halo model is able to reproduce nonlinear WDM power spectra with the same accuracy as can currently be achieved for CDM.

6 CONCLUSION

In this paper we have explored nonlinear structure formation in the WDM cosmological model, through a large suite of cosmological N-body simulations and through the halo model. The study was done for a set of fully thermalized WDM models with particle masses in the set $m = \{0.25, 0.5, 0.75, 1.0, 1.25\}$keV. These masses range from purely pedagogical models, towards more realistic scenarios for the dark particle.

For the simulations we chose a box size $L = 256\,h^{-1}$Mpc, which was small enough to resolve both the small scales, where WDM effects play an important role, and the large scales, which are required for correct linear evolution of the box-modes. All models were simulated with $N = \{256^3, 512^3, 1024^3\}$ particles. This was done in order to disentangle physical effects from numerical ones.

In the original halo model calculation for WDM by Smith & Markovic (2011), it was shown that in order to make robust predictions, one requires good understanding of dark matter halo profiles, the mass function and halo bias. In this work we performed a detailed study of all of these ingredients. Our findings can be summarized as follows:

(i) Mass function: Below a certain scale, the WDM mass function is suppressed with respect to CDM. This suppression is considerably stronger than that obtained by simply applying the Sheth-Tormen approach together with the linear power spectrum of WDM. In agreement with Smith & Markovic (2011), we found that the mass functions for the different WDM models could be transformed into a single locus of points. This was achieved by taking the ratio of the WDM mass function with that for CDM, and then rescaling the masses by $M_{\rm hm}$ (or equivalently $M_{\rm fs}$). We used a fitting function similar to that proposed in Dunstan et al. (2011) to link the Sheth-Tormen mass function to the measured one. The fitting function, which has only one free parameter, was able to reproduce all of the data with an accuracy of a few percent. We also found a strong boost in the mass function at very small mass scales. We showed that this was consistent with artificial halo formation around the initial particle lattice (cf. Wang & White 2007).

(ii) Halo bias: We measured the linear halo bias, using the four largest modes in our simulations. For smaller mass haloes, we found a small enhancement of the bias in WDM simulations, which was qualitatively consistent with the predictions of Smith & Markovic (2011). However, owing to the simulation box being too small, we were unable to quantify this more robustly. At very small masses we found a prominent boost in the bias. We found that this was again a sign of artificial halo formation.

(iii) Density profiles: In the CDM model, the density profiles of dark matter haloes can be characterized by an NFW profile, with a monotonically decreasing concentration-mass relation. In the WDM scenario, we have shown that the NFW profile remains valid for the models and resolution limits of our simulations, and we saw no evidence for a central density core. A simple adaption of the CDM concentration-mass relation, would suggest a strong flattening towards small masses. Whilst, we found such a flattening, the measurements in fact revealed a turnover towards smaller masses. This somewhat surprising result may be interpreted as a sign of top-down structure formation. We modelled the mean relation by adapting a fitting formula similar to that for the mass function. Our fit to the $c(M)$ data was good to an accuracy of $\sim 10\%$. Interestingly, we found that the deviations from CDM in the WDM model, appear in the $c(M)$ relation for halo masses one order of magnitude larger than for the mass function.

After analyzing these ingredients in detail and developing new fitting functions for them, we were able to improve the small-scale performance of the WDM halo model. We found that for $k \gtrsim 3\,h\,{\rm Mpc}^{-1}$, we could predict the absolute amplitude of the power spectrum to better than $\sim 10\%$. However, we were able to predict the ratio of the WDM to CDM spectra, at better than $\lesssim 2\%$. This was competitive with the latest fitting formulae (Viel et al. 2011).

One of the many advantages of the halo model based approach, is that we may more confidently extrapolate our power spectra predictions to smaller scales than can be done from a fitting formula, since the model is built on physical quantities. Furthermore, we may also use the model to study the clustering of galaxies (Zehavi et al. 2005). It is hoped that this may lead to a method for constraining WDM models from galaxy clustering studies. Lastly, one further issue for future study, is to establish a better theoretical understanding of what shapes the mass function and halo concentrations in WDM. In particular, in finding the turnover in the concentration mass relation, have we really seen the reversal of bottom-up structure formation. This promises to be an interesting future challenge.

ACKNOWLEDGMENTS

It is a pleasure to thank Donnino Anderhalden, Jürg Diemand and Darren Reed for useful discussions. We also thank Doug Potter and Joachim Stadel for use of their power spectrum code and technical support concerning `pkdgrav`. We thank Roman Scoccimarro for making public his `2LPT` code. AS, RES and BM acknowledge support from the Swiss National Foundation. RES also acknowledges support from a Marie Curie Reintegration Grant and the Alexander von Humboldt Foundation.

REFERENCES

Avila-Reese, V., Colín, P., Valenzuela, O., D'Onghia, E., & Firmani, C. 2001, ApJ, 559, 516
Bardeen, J. M., Bond, J. R., Kaiser, N., & Szalay, A. S. 1986, ApJ, 304, 15
Blumenthal, G. R., Faber, S. M., Primack, J. R., & Rees, M. J. 1984, Nature, 311, 517
Bode, P., Ostriker, J. P., & Turok, N. 2001, ApJ, 556, 93
Bond, J. R., Cole, S., Efstathiou, G., & Kaiser, N. 1991, ApJ, 379, 440
Bond, J. R. & Szalay, A. S. 1983, ApJ, 274, 443
Boyanovsky, D. 2010, ArXiv e-prints
Boyarsky, A., Iakubovskyi, D., Ruchayskiy, O., & Savchenko, V. 2008, MNRAS, 387, 1361
Boyarsky, A., Lesgourgues, J., Ruchayskiy, O., & Viel, M. 2009a, Journal of Cosmology and Astro-Particle Physics, 5, 12
—. 2009b, Physical Review Letters, 102, 201304
Bullock, J. S., Kolatt, T. S., Sigad, Y., Somerville, R. S., Kravtsov, A. V., Klypin, A. A., Primack, J. R., & Dekel, A. 2001, MNRAS, 321, 559
Bullock, J. S., Kravtsov, a. A. V., & Colín, P. 2002, ApJL, 564, L1
Cole, S. & Kaiser, N. 1989, MNRAS, 237, 1127
Cole, S., Percival, W. J., Peacock, J. A., & The 2dFGRS Team. 2005, MNRAS, 362, 505
Colín, P., Avila-Reese, V., & Valenzuela, O. 2000, ApJ, 542, 622
Colín, P., Valenzuela, O., & Avila-Reese, V. 2008, ApJ, 673, 203
Colombi, S., Dodelson, S., & Widrow, L. M. 1996, ApJ, 458, 1
Cooray, A. & Sheth, R. 2002, Phys. Rep. , 372, 1
Crocce, M., Pueblas, S., & Scoccimarro, R. 2006, MNRAS, 373, 369

Davis, M., Efstathiou, G., Frenk, C. S., & White, S. D. M. 1985, ApJ, 292, 371

de Blok, W. J. G., Walter, F., Brinks, E., Trachternach, C., Oh, S.-H., & Kennicutt, Jr., R. C. 2008, Astron. Journal, 136, 2648

de Vega, H. J. & Sanchez, N. G. 2010, MNRAS, 404, 885

de Vega, H. J. & Sanchez, N. G. 2011, ArXiv e-prints

Diemand, J. & Kuhlen, M. 2008, ApJL, 680, L25

Diemand, J., Moore, B., & Stadel, J. 2004, MNRAS, 353, 624

Dodelson, S. & Widrow, L. M. 1994, Physical Review Letters, 72, 17

Dunstan, R. M., Abazajian, K. N., Polisensky, E., & Ricotti, M. 2011, ArXiv e-prints

Ellis, J., Hagelin, J. S., Nanopoulos, D. V., Olive, K., & Srednicki, M. 1984, Nuclear Physics B, 238, 453

Gentile, G., Famaey, B., Zhao, H., & Salucci, P. 2009, Nature, 461, 627

Gorbunov, D., Khmelnitsky, A., & Rubakov, V. 2008, Journal of High Energy Physics, 12, 55

Jungman, G., Kamionkowski, M., & Griest, K. 1996, Phys. Rep. , 267, 195

Kawasaki, M., Sugiyama, N., & Yanagida, T. 1997, Modern Physics Letters A, 12, 1275

Klypin, A., Kravtsov, A. V., Valenzuela, O., & Prada, F. 1999, ApJ, 522, 82

Kolb, E. W. & Turner, M. S. 1990, The early universe. (Addison Wesley, 1990)

Komatsu, E., Smith, K. M., Dunkley, J., & The WMAP Team. 2011, ApJS, 192, 18

Kuzio de Naray, R., Martinez, G. D., Bullock, J. S., & Kaplinghat, M. 2010, ApJL, 710, L161

Lewis, A., Challinor, A., & Lasenby, A. 2000, Astrophys. J., 538, 473

Lovell, M., Eke, V., Frenk, C., Gao, L., Jenkins, A., Theuns, T., Wang, J., Boyarsky, A., & Ruchayskiy, O. 2011, ArXiv e-prints

Macciò, A. V., Dutton, A. A., & van den Bosch, F. C. 2008, MNRAS, 391, 1940

Macciò, A. V., Dutton, A. A., van den Bosch, F. C., Moore, B., Potter, D., & Stadel, J. 2007, MNRAS, 378, 55

Macciò, A. V. & Fontanot, F. 2010, MNRAS, 404, L16

Markovic, K., Bridle, S., Slosar, A., & Weller, J. 2010, ArXiv e-prints

Miranda, M. & Macciò, A. V. 2007, MNRAS, 382, 1225

Mo, H. J. & White, S. D. M. 1996, MNRAS, 282, 347

Moore, B., Quinn, T., Governato, F., Stadel, J., & Lake, G. 1999, MNRAS, 310, 1147

Moroi, T., Murayama, H., & Yamaguchi, M. 1993, Physics Letters B, 303, 289

Navarro, J. F., Frenk, C. S., & White, S. D. M. 1997, ApJ, 490, 493

Neto, A. F., Gao, L., Bett, P., Cole, S., Navarro, J. F., Frenk, C. S., White, S. D. M., Springel, V., & Jenkins, A. 2007, MNRAS, 381, 1450

Peebles, P. J. E. 1982, ApJL, 263, L1

—. 2001, ApJ, 557, 495

Peebles, P. J. E. & Nusser, A. 2010, Nature, 465, 565

Polisensky, E. & Ricotti, M. 2010, ArXiv e-prints

Prada, F., Klypin, A. A., Cuesta, A. J., Betancort-Rijo, J. E., & Primack, J. 2011, ArXiv e-prints

Press, W. H. & Schechter, P. 1974, ApJ, 187, 425

Salucci, P., Lapi, A., Tonini, C., Gentile, G., Yegorova, I., & Klein, U. 2007, MNRAS, 378, 41

Scoccimarro, R. 1998, MNRAS, 299, 1097

Seljak, U., Makarov, A., McDonald, P., & Trac, H. 2006, Physical Review Letters, 97, 191303

Shaposhnikov, M. & Tkachev, I. 2006, Physics Letters B, 639, 414

Sheth, R. K. & Tormen, G. 1999, MNRAS, 308, 119

Smith, R. E., Desjacques, V., & Marian, L. 2011, PRD, 83, 043526

Smith, R. E. & Markovic, K. 2011, ArXiv e-prints

Smith, R. E., Scoccimarro, R., & Sheth, R. K. 2007, PRD, 75, 063512

Smith, R. E., Peacock, J. A., Jenkins, A., White, S. D. M., Frenk, C. S., Pearce, F. R., Thomas, P. A., Efstathiou, G. & Couchman, H. M. P. 2007, MNRAS, 341, 1311

Springel, V. 2005, MNRAS, 364, 1105

Springel, V., Wang, J., Vogelsberger, M., Ludlow, A., Jenkins, A., Helmi, A., Navarro, J. F., Frenk, C. S., & White, S. D. M. 2008, MNRAS, 391, 1685

Stadel, J., Potter, D., Moore, B., Diemand, J., Madau, P., Zemp, M., Kuhlen, M., & Quilis, V. 2009, MNRAS, 398, L21

Stadel, J. G. 2001, PhD thesis, AA(UNIVERSITY OF WASHINGTON)

Swaters, R. A., Madore, B. F., van den Bosch, F. C., & Balcells, M. 2003, ApJ, 583, 732

Tegmark, M., , & The SDSS Team. 2006, PRD, 74, 123507

Tikhonov, A. V., Gottlöber, S., Yepes, G., & Hoffman, Y. 2009, MNRAS, 399, 1611

Tinker, J. L., Robertson, B. E., Kravtsov, A. V., Klypin, A., Warren, M. S., Yepes, G., & Gottlöber, S. 2010, ApJ, 724, 878

Tremaine, S. & Gunn, J. E. 1979, Physical Review Letters, 42, 407

Viel, M., Lesgourgues, J., Haehnelt, M. G., Matarrese, S., & Riotto, A. 2005, PRD, 71, 063534

Viel, M., Markovic, K., Baldi, M., & Weller, J. 2011, ArXiv e-prints

Villaescusa-Navarro, F. & Dalal, N. 2011, Journal of Cosmology and Astro-Particle Physics, 3, 24

Wang, J. & White, S. D. M. 2007, MNRAS, 380, 93

White, M. & Croft, R. A. C. 2000, ApJ, 539, 497

Zavala, J., Jing, Y. P., Faltenbacher, A., Yepes, G., Hoffman, Y., Gottlöber, S., & Catinella, B. 2009, ApJ, 700, 1779

Zehavi, I., Zheng, Z., Weinberg, D. H., Frieman, J. A., Berlind, A. A., Blanton, M. R., Scoccimarro, R., Sheth, R. K., Strauss, M. A., Kayo, I., Suto, Y., Fukugita, M., Nakamura, O., Bahcall, N. A., Brinkmann, J., Gunn, J. E., Hennessy, G. S., Ivezić, Ž., Knapp, G. R., Loveday, J., Meiksin, A., Schlegel, D. J., Schneider, D. P., Szapudi, I., Tegmark, M., Vogeley, M. S., York, D. G., & SDSS Collaboration. 2005, ApJ, 630, 1

Zentner, A. R. & Bullock, J. S. 2003, ApJ, 598, 49